ROYAL SOCIETY
OF CHEMISTRY

PAPER

Check for updates

Growth, characterization and theoretical analysis of α-SrGeO₃ as a candidate mid-IR stimulated Raman scattering crystal†

Hailong Wang,‡[ab] Bin Li,‡[ab] Ying Zhou,[c] Guimei Zheng,[b] Xue Zhang[b] and Songming Wan [ID] *[bd]

The α-BaGeO₃ crystal is a potential stimulated Raman scattering (SRS) medium for use in generating lasers at wavelengths in the range of 2.1–2.4 μm. However, the growth of a large-sized and high-quality α-BaGeO₃ crystal is still challenging. Here, we turn the attention to its analogue, α-SrGeO₃. The α-SrGeO₃ crystal was grown by the high-temperature solution method under conditions similar to those for growth of α-BaGeO₃. The grown α-SrGeO₃ single crystals have larger sizes (approximately 8 × 12 × 10 mm³) and higher quality than α-BaGeO₃. A strong Raman peak at 813 cm⁻¹ and a wide transparent window from 0.22 to 5.78 μm indicate that the α-SrGeO₃ crystal is a promising SRS crystal working in the 2.1–2.4 μm wavelength range. From density functional theory (DFT) computations, the strongest Raman peak, the ultraviolet cut-off edge and the infrared cut-off edge of α-SrGeO₃ are all related to the $[Ge_3O_9]^{6-}$ ring, the basic building unit in both α-SrGeO₃ and α-BaGeO₃, which suggests that the $[Ge_3O_9]^{6-}$ ring is a valuable structural group for developing new mid-IR SRS crystals.

Introduction

Lasers at wavelengths in the range of 2.1–2.4 μm have excellent atmospheric penetrability and eye safety, and also overlap with the characteristic absorption bands of many air pollutants,[1–4] making them suitable for various applications, including laser ranging, remote sensing, environmental monitoring and free-space communication.[3–7] A simple and effective method to generate the 2.1–2.4 μm lasers is by use of the stimulated Raman scattering (SRS) effect in crystal.[8–11] Our previous work has revealed that the low-temperature phase BaGeO₃ (α-BaGeO₃) crystal is a promising SRS crystal for use in the range of 2.1–2.4 μm due to its strong Raman response and wide infrared transparent window.[12] In order to circumvent the phase transition,[13] the α-BaGeO₃ crystal has to be grown by the high-temperature solution method.[12] Although considerable effort has been

devoted, the growth of large-sized, high-quality α-BaGeO₃ crystals remains difficult. A problem frequently encountered is that small α-BaGeO₃ crystal plates are apt to form and float on the solution surface, which influences the crystal growth and ultimately deteriorates the crystal quality.

Crystal growth in a high-temperature solution begins with the desolvation of crystal growth units (also the building units of the crystal in most cases[14,15]) achieved by slowly cooling the solution or evaporating the solvent. Then, the growth units are transported to the crystal–solution interface by diffusion, natural and forced convection (usually, the forced convection is the main contribution), and eventually integrated into the crystal by an interface kinetic process.[16] Only when the integrated rate of the growth unit into the crystal exceeds the transport rate and the transport rate exceeds the desolvation rate is the crystal growth stable. In our experiments for growth of the α-BaGeO₃ crystal, the desolvation rates are rather low (the cooling rates are less than 1.0 °C per day) and the forced convection is sufficient to transport the growth units (the maximal crystal rotational rates are 20 rotations per minute), therefore, we deem that the interface kinetic process is the key step to influence the α-BaGeO₃ crystal growth.

The interface kinetic process of the α-BaGeO₃ crystal growth is depicted in Fig. 1. The α-BaGeO₃ crystal is a pseudo-wollastonite-type structure alternately stacked by the layer of the Ba²⁺ cation and the layer of the $[Ge_3O_9]^{6-}$ ring.[12] During the crystal growth, the $[Ge_3O_9]^{6-}$ ring in the solution (the growth unit) is absorbed onto the crystal–solution interface by the Ba²⁺

[a] *University of Science and Technology of China, Hefei 230026, China*

[b] *Anhui Provincial Key Laboratory of Photonics Devices and Materials, Anhui Institute of Optics and Fine Mechanics, HFIPS, Chinese Academy of Sciences, Hefei 230031, China. E-mail: smwan@aiofm.ac.cn*

[c] *Institutes of Physical Science and Information Technology, Anhui University, Hefei 230601, China*

[d] *Advanced Laser Technology Laboratory of Anhui Province, Hefei 230037, China*

† Electronic supplementary information (ESI) available: Synthesis of polycrystalline raw materials for growth of the α-SrGeO₃ crystal, convergence tests for the total energy of α-SrGeO₃, and the crystal vibrational modes and their corresponding frequencies. See DOI: https://doi.org/10.1039/d4tc03340j

‡ H. Wang and B. Li contributed equally in this work.

17122 | *J. Mater. Chem. C,* 2024, **12**, 17122–17127
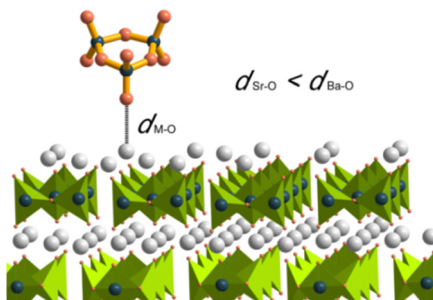
This journal is © The Royal Society of Chemistry 2024

Fig. 1 Illustration of the kinetic process occurring near the α-BaGeO$_3$ (or α-SrGeO$_3$) crystal–solution interface (M = Ba or Sr).

cation at the interface, and *vice versa*. The absorbed strength determines the rate of the growth unit integrated into the crystal.[17] Owing to the large size, the Ba^{2+} cation weakly bonds to the [Ge$_3$O$_9$]$^{6-}$ ring, which brings about a low crystal growth rate. As a result, numerous growth units that fail to precipitate on the interface organize them into new crystal nuclei and finally destroy the single crystal growth.

The low-temperature phase SrGeO$_3$ (α-SrGeO$_3$) crystal has a structure very similar to that of the α-BaGeO$_3$ crystal. It is also the pseudo-wollastonite-type structure and crystallizes in the monoclinic $C2/c$ space group with the unit cell parameters (a = 12.533(3) Å, b = 7.262(1) Å, c = 11.259(3) Å, β = 111.30(2)° and Z = 12) close to those of the α-BaGeO$_3$ crystal (a = 13.178(10) Å, b = 7.626(6) Å, c = 11.670(9) Å, β = 111.638(8)° and Z = 12). The α-SrGeO$_3$ crystal is built up of Sr^{2+} cations and [Ge$_3$O$_9$]$^{6-}$ rings.[18] As compared with Ba^{2+}, Sr^{2+} has a smaller size and thus a stronger interaction with the [Ge$_3$O$_9$]$^{6-}$ ring. On the base of the foregoing analysis regarding the interface kinetics of the α-BaGeO$_3$ crystal growth, we believe that, under similar conditions, the integrated rate of the growth units into the α-SrGeO$_3$ crystal is larger than that into the α-BaGeO$_3$ crystal, and thus the spontaneous nucleation likely to occur in the α-SrGeO$_3$ crystal growth can be suppressed. Due to the structural similarity, the α-SrGeO$_3$ crystal is expected to exhibit similar spectral performances to those of the α-BaGeO$_3$ crystal, that is, the α-SrGeO$_3$ crystal also has good spectral characteristics as an SRS crystal for use in the range of 2.1–2.4 μm. Furthermore, like α-BaGeO$_3$ which is stable below 1100 °C,[19] the α-SrGeO$_3$ crystal remains stable below 1020 °C.[20]

In this study, we use the high-temperature solution method to grow the α-SrGeO$_3$ crystal under conditions similar to those for growth of the α-BaGeO$_3$ crystal to verify that the α-SrGeO$_3$ crystal has a growth performance superior to the α-BaGeO$_3$ crystal. Raman and transmission spectra of the α-SrGeO$_3$ crystal are studied by experimental and theoretical approaches to evaluate its potential as an SRS crystal.

Experimental and computational methods

Single crystal growth

Owing to the phase transition, the α-SrGeO$_3$ crystal has to be grown by the high-temperature solution method.[16] For comparison, the conditions for growth of the α-BaGeO$_3$ crystal were applied to grow the α-SrGeO$_3$ crystal. The crystal growth raw materials, polycrystalline α-SrGeO$_3$ and NaBO$_2$ (the flux), were synthesized through solid-state reactions (see the ESI† for more details). The raw materials were mixed with a molar ratio of n(α-SrGeO$_3$) : n(NaBO$_2$) = 1 : 1.25, loaded into a platinum crucible, and then placed in a crystal growth furnace. After the raw materials were completely melted, an α-SrGeO$_3$ seed crystal was immersed in the solution to determine the saturation temperature. Once the temperature was determined, another seed crystal with the direction perpendicular to the (001) plane was employed to grow the α-SrGeO$_3$ crystal, with a cooling rate of 0.5–1.0 °C per day and a crystal rotational rate of 5–20 rotations per minute. One month later, the growth was ended. The grown α-SrGeO$_3$ crystal was cut. One part was crushed into powder for X-ray diffraction (XRD) measurement; another part was polished into a crystal plate for collecting Raman and transmission spectra.

Powder X-ray diffraction

The XRD pattern of the powder was recorded at room temperature on a Rigaku TTRAX-III X-ray powder diffractometer equipped with the Cu $K\alpha$ radiation (λ = 1.54056 Å). Diffraction data were collected in the 2θ range from 10 to 70° with a step width of 0.02°.

Raman spectroscopy

Raman spectra of the α-SrGeO$_3$ and α-BaGeO$_3$ crystals were recorded on a Renishaw inVia-Reflex Raman spectrometer with a backscattering configuration. A Q-switched SHG Nd:YAG laser, with a wavelength at 532 nm and a power of 10 mW, was utilized as the excitation resource. The spectral data were collected in the frequency range from 100 to 4000 cm^{-1} with a resolution less than 1.5 cm^{-1}. Before each experiment, the frequency was calibrated by a single-crystal silicon wafer.

Transmission spectroscopy

A 3-mm-thick α-SrGeO$_3$ crystal plate was employed to collect transmission spectra. The UV-Vis-NIR transmission spectrum was recorded on a PerkinElmer Lambda-900 UV-Vis-NIR spectrophotometer in the wavelength range from 0.19 to 2.5 μm, and the IR spectrum was recorded by using a Gangdong FTIR-650G spectrophotometer in the wavelength range from 2.5 to 25 μm.

Computational methods

The Raman spectrum and electronic structure of the α-SrGeO$_3$ crystal were studied by the density functional theory (DFT) method,[21] which were implemented in the Cambridge serial total energy package (CASTEP).[22] The crystal structure of α-SrGeO$_3$ reported by Nishi was adopted as the structural model.[18] The local density approximation (LDA) in the Perdew and Zunger parameterization of the numerical results of Ceperley and Alder (CA-PZ) was selected to treat the exchange–correlation energy.[23] The norm-conserving pseudo-potential was used to describe the interaction between ionic cores and valence electrons.[24] The valence electron configurations of strontium, germanium and oxygen were 4s^{2}4p^{6}5s^2, 4s^{2}4p^2 and

This journal is © The Royal Society of Chemistry 2024

J. Mater. Chem. C, 2024, **12**, 17122–17127 | 17123

$2s^2 2p^4$, respectively. The convergence criteria of the total energy change, displacement, force and stress for the structural optimization were 10^{-5} eV per atom, 0.001 Å, 0.03 eV Å^{-1} and 0.05 GPa, respectively. According to convergence tests, a k-point grid of $1 \times 2 \times 1$ and an energy cutoff of 1000 eV were sufficient to ensure the total energy convergence to within 1 meV per atom (Table S1 and Fig. S3, ESI†). The computational Raman peak intensities were corrected using the Bose–Einstein factors calculated with the wavelength of the excitation resource (532 nm) and the room temperature of 300 K.[25] All of the Raman lines were broadened by the Lorentzian line-shape function with a fixed full width at half maximum (FWHM) of 10 cm^{-1}.[26] The Heyd–Scuseria–Ernzerhof 06 (HSE06) screened hybrid functional was employed to compute the electronic structure of the α-SrGeO$_3$ crystal.[27,28] The optimized structural model and parameters for computation of the crystal Raman spectrum were adopted in the electronic structure computation.

Results and discussion

Single crystal growth

A typical α-SrGeO$_3$ crystal is present in Fig. 2a. The crystal is made up of two single crystals (twin crystals), with regular shapes and characterized by the hexagonal (001) end faces. The two single crystal sizes are about $8 \times 12 \times 10$ mm^3. Fig. 2c shows the powder XRD of the crystal. All the diffraction peaks are consistent with those in the standard pattern of α-SrGeO$_3$ (JCPDS no. 87–469), indicating that the crystal is α-SrGeO$_3$. For comparison, an α-BaGeO$_3$ crystal grown under similar conditions [the same flux (NaBO$_2$), flux concentration, seed crystal direction, cooling rate and crystal rotational rate] is shown in Fig. 2b. The crystal is made up of five single crystals, and thus

exhibits a more complex external shape. Each of the single crystals is also characterized by the hexagonal (001) end faces; yet their sizes are smaller than that of the α-SrGeO$_3$ single crystals. Suffering from the multiple twinning effect and the resulting crystal boundaries and inclusions, the α-BaGeO$_3$ crystal quality is inferior to the α-SrGeO$_3$ crystal. As we expected, the growth performance of the α-SrGeO$_3$ crystals is superior to that of the α-BaGeO$_3$ crystal.

Raman spectral characteristics

The experimental Raman spectrum of the α-SrGeO$_3$ crystal is shown in Fig. 3. At least 13 Raman peaks are observable, but only one significantly strong and narrow peak, located at 813 cm^{-1}, is present in the spectrum. This spectral characteristic is beneficial for generating SRS lasers. For comparison, the Raman spectrum of the α-BaGeO$_3$ crystal was recorded under the same conditions. The two spectra are very similar (Fig. 3). The intensity and FWHM of the strongest 813 cm^{-1} peak of α-SrGeO$_3$ are comparable to those of the strongest 808 cm^{-1} peak of α-BaGeO$_3$. Therefore, the α-SrGeO$_3$ crystal also has a strong Raman response, as with the α-BaGeO$_3$ crystal.[12]

The DFT computation reveals that the α-SrGeO$_3$ crystal has 90 vibrational modes ($20A_g + 23A_u + 22B_g + 25B_u$), including three acoustic modes ($A_u + 2B_u$), 42 Raman active modes ($20A_g + 22B_g$), and 45 IR active modes ($22A_u + 23B_u$) (Table S2 in the ESI†). The computational Raman spectrum is shown in Fig. 4a, which is in good agreement with the experimental one both in frequency and in intensity. On the base of the computational result, two important crystal characteristic peaks, located at 476 and 813 cm^{-1} (experimental values), are assigned. The 476 cm^{-1} peak originates from the breathing vibration of the three bridge oxygen atoms in the $[Ge_3O_9]^{6-}$ ring; the 813 cm^{-1} peak arises from the symmetrical stretching vibration of the six extra-ring Ge–O bonds (Fig. 4b). Benefiting from the synergistic vibrational effect, the 813 cm^{-1} peak has a strong Raman response. The other characteristic Raman peaks of the α-SrGeO$_3$ crystal are also attributed to the vibrations of the
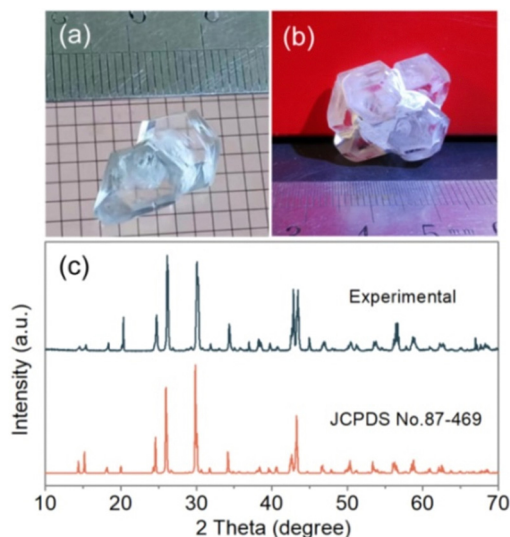

Fig. 2 (a) α-SrGeO$_3$ single crystals grown by the high-temperature solution method, (b) α-BaGeO$_3$ single crystals grown under similar conditions and (c) the powder XRD pattern of the α-SrGeO$_3$ crystal, with the standard XRD pattern.
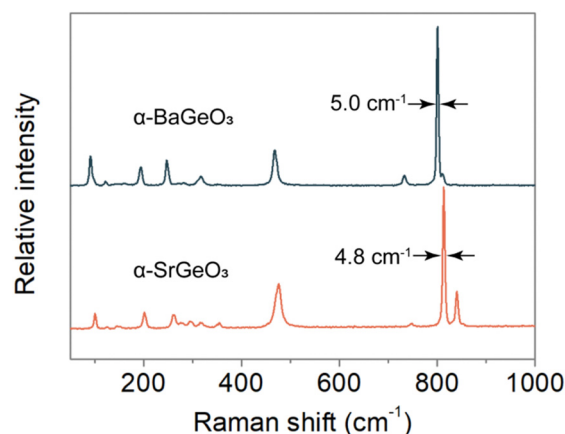

Fig. 3 Experimental Raman spectra of the α-SrGeO$_3$ and the α-BaGeO$_3$ crystal. The FWHMs of the α-SrGeO$_3$ 813 cm^{-1} peak and the α-BaGeO$_3$ 808 cm^{-1} peak are 4.8 cm^{-1} and 5.0 cm^{-1}, respectively.

17124 | J. Mater. Chem. C, 2024, 12, 17122–17127
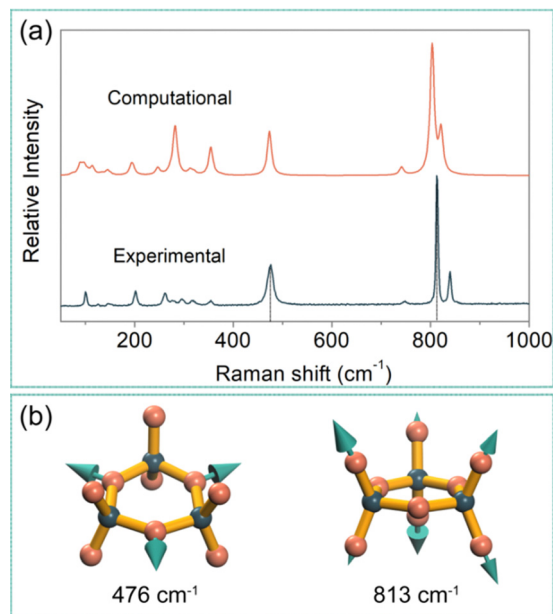
This journal is © The Royal Society of Chemistry 2024

Fig. 4 (a) Experimental and computational Raman spectra of the α-SrGeO₃ crystal and (b) two characteristic vibrational modes of the crystal.

$[Ge_3O_9]^{6-}$ ring (Fig. S4 in the ESI†). These results are consistent with the computational results of α-BaGeO₃,[12] and manifest

that the Raman spectral similarity between α-SrGeO₃ and α-BaGeO₃ is due to their structural similarity.

UV-Vis-NIR transmission spectral characteristics

The UV-Vis-NIR transmission spectrum of the α-SrGeO₃ crystal is shown in Fig. 5a. The UV cut-off edge is located at 0.22 μm; the transmittance is greater than 70% from 1.2 to 2.5 μm. Therefore, the crystal is suitable for application in the range of 2.1–2.4 μm. Moreover, we employed the Tauc plot method to evaluate the crystal bandgap.[29,30] The absorption plot of $(\alpha h\nu)^{1/2}$ versus photon energy ($h\nu$), derived from the UV-Vis-NIR transmission spectrum, is displayed in Fig. 5b, which results in an experimental bandgap at 5.20 eV.

The UV absorption is related to the electronic transition from the valence band (VB) top to the conduction band (CB) bottom.[31] The computational band structure of the α-SrGeO₃ crystal is presented in Fig. 5c. The VB top and CB bottom have different k-points, revealing its indirect bandgap nature. The computational bandgap (5.126 eV) is very close to the experimental value (5.20 eV). Fig. 5d shows the total and partial densities of states (TDOS and PDOSs) of the α-SrGeO₃ crystal. The VB top and CB bottom are mainly composed of the O-2p state and Ge-4s state, respectively, indicating that the UV absorption of the α-SrGeO₃ crystal is ascribed to the electronic transition from the O-2p to the Ge-4s state.
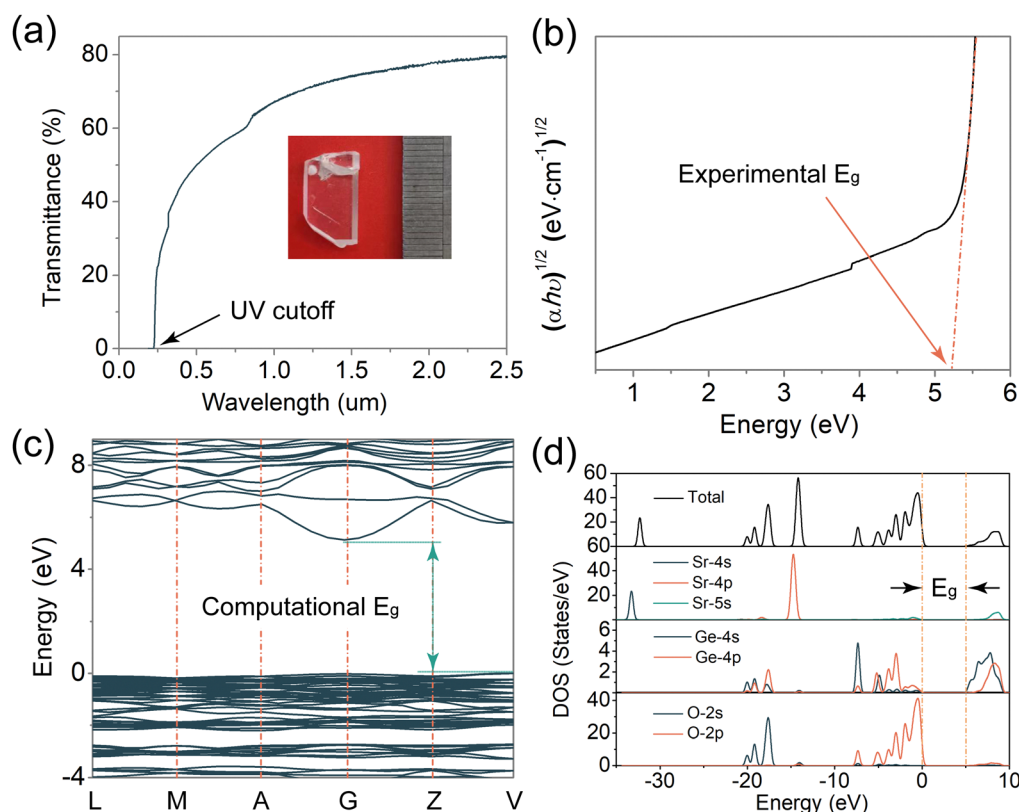

Fig. 5 (a) A UV-Vis-IR transmission spectrum of the α-SrGeO₃ crystal [the inset is the α-SrGeO₃ crystal plate (16 × 9 × 3 mm³) for the spectrum measurement], (b) a plot of $(\alpha h\nu)^{1/2}$ versus $h\nu$ for the crystal, (c) the band structure of the crystal and (d) TDOS and PDOSs of the crystal.
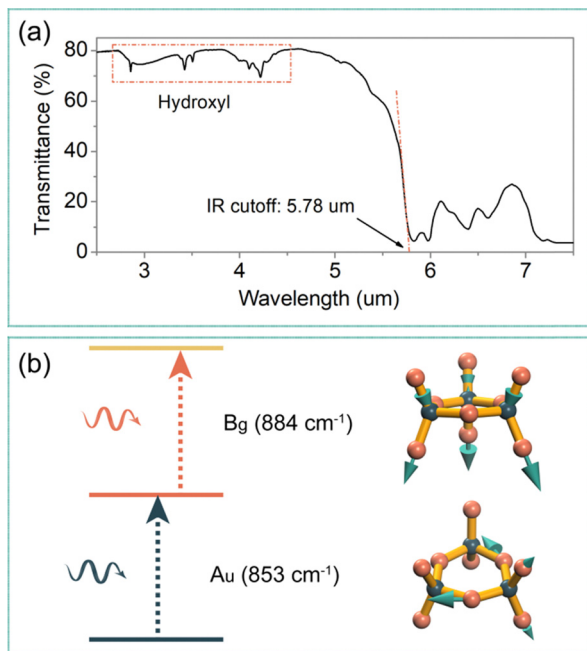
This journal is © The Royal Society of Chemistry 2024

J. Mater. Chem. C, 2024, **12**, 17122–17127 | **17125**

Fig. 6 (a) A mid-IR transmission spectrum of the α-SrGeO₃ crystal and (b) the highest-frequency A_u and B_g modes.

IR transmission spectral characteristics

As shown in Fig. 6a, the α-SrGeO$_3$ crystal is highly transparent from 2.5 to 5 µm, which allows the crystal to extend its application to the mid-IR range. It is worth noting that a few weak absorption peaks are present from 2.7 to 4.5 µm. These peaks can be assigned to the vibrations of hydroxyl,[32] which implies that the crystal is weakly hygroscopic. As a result, the surface was hydrolysed when the crystal was placed in air for a long time or cut/polished in a watery environment. However, the hydrolysis can be avoided if the crystal is stored in a dryer and processed under a water-free condition.

The IR cut-off edge of the α-SrGeO$_3$ crystal is at 5.78 µm (Fig. 6a), close to that of α-BaGeO$_3$ (5.9 µm).[12] In general, the IR cut-off edge corresponds to the highest-frequency second-order IR-active modes.[33] The α-SrGeO$_3$ crystal has the C_2 point group symmetry. Its second-order IR-active mode is the coupled mode that combines an A_u mode with a B_g mode ($A_u \otimes B_g$).[34] According to the DFT computation, the highest frequencies of the A_u and the B_g modes of α-SrGeO$_3$ are 853 cm^{-1} and 884 cm^{-1} (Table S2 in the ESI†), respectively. Therefore, the highest frequency of the $A_u \otimes B_g$ mode is 1737 cm^{-1}, which corresponds to an IR absorption wavelength of 5.76 µm. The computational wavelength is very close to the experimental IR cut-off edge, which manifests that the IR cut-off edge arises from the combination of the 853 cm^{-1} and 884 cm^{-1} modes (Fig. 6b).

Conclusions

The α-SrGeO$_3$ crystal growth is dominated by an interface kinetic process. The stronger bonding between the Sr^{2+} cation and the [Ge$_3$O$_9$]$^{6-}$ ring can improve the single-crystal size and the crystal quality. Under the conditions that were adopted to grow the α-BaGeO$_3$ crystal, α-SrGeO$_3$ single crystals with sizes of about $8 \times 12 \times 10$ mm^3 were obtained. The multiple-twinning effect was suppressed. The α-SrGeO$_3$ crystal has a strong Raman response, comparable to that of the α-BaGeO$_3$ crystal, and a wide transparent window ranging from 0.22 to 5.78 µm. These experimental results confirm that the α-SrGeO$_3$ crystal is a promising SRS medium for use in the mid-IR range, including the 2.1–2.4 µm range. According to the DFT computations, the primary spectral characteristics of the α-SrGeO$_3$ crystal are determined by the [Ge$_3$O$_9$]$^{6-}$ ring. The strongest Raman peak originates from the symmetric stretching vibration of the six extra-ring Ge–O bonds; the UV cut-off edge is ascribed to the electronic transition from the O-2p to the Ge-4s state, within the ring; the IR cut-off edge corresponds to the highest-frequency $A_u \otimes B_g$ mode, arising from the vibrations of the ring. The computational results reveal that the [Ge$_3$O$_9$]$^{6-}$ ring is a good structural group for exploring new IR SRS crystals.

Author contributions

H. W. and B. L. performed the crystal growth and the DFT computations. Y. Z. and S. W. conducted the spectral measurements. S. W. initiated and supervised the work. All authors participated in the discussion.

Data availability

The data supporting this article have been included as part of the ESI.†

Conflicts of interest

There are no conflicts to declare.

Acknowledgements

Notes and references

1 H. Horvath, *Atmos. Environ.*, 1993, **27**, 293–317.
2 S. W. Henderson, C. P. Hale, J. R. Magee, M. J. Kavaya and A. V. Huffaker, *Opt. Lett.*, 1991, **16**, 773–775.
3 *Mid-infrared Coherent Sources and Applications*, ed. M. Ebrahim-Zadeh and I. T. Sorokina, Springer, Netherlands, 2008.
4 R. L. Byer, *Science*, 1988, **239**, 742–747.

17126 | *J. Mater. Chem. C*, 2024, **12**, 17122–17127

This journal is © The Royal Society of Chemistry 2024

5 S. D. Jackson, *Nat. Photonics*, 2012, **6**, 423–431.

6 K. Scholle, S. Lamrini, P. Koopmann and P. Fuhrberg, in *Frontiers in Guided Wave Optics and Optoelectronics*, ed. B. Pal, INTECH, *Croati*, 2010, pp. 471–500.

7 J. G. Daly and C. A. Smith, 2.0-micron laser applications, *Proc. SPIE*, 1992, **1627**, 26–31.

8 P. Černý, H. Jelínková, P. G. Zverev and T. T. Basiev, *Prog. Quant. Electron.*, 2004, **28**, 113–143.

9 J. Q. Zhao, Y. Li, S. Zhang, L. Li and X. L. Zhang, *Opt. Express*, 2015, **23**, 10075–10080.

10 U. Sheintop, D. Sebbag, P. Komm, S. Pearl, G. Marcus and S. Noach, *Opt. Express*, 2019, **27**, 17112–17121.

11 E. Perez, U. Sheintop, R. Nahear, G. Marcus and S. Noach, *Opt. Lett.*, 2020, **45**, 5409–5412.

12 S. M. Wan, Y. Zeng, Y. N. Yao, M. R. D. Mutailipu, J. Han, S. J. Jiang, S. J. Zhang and S. L. Pan, *Inorg. Chem.*, 2020, **59**, 3542–3545.

13 D. M. Többens, V. Kahlenberg, C. Gspan and G. Kothleitner, *Acta Crystallogr., Sect. B: Struct. Sci.*, 2006, **62**, 1002–1009.

14 S. J. Zhang, S. M. Wan, Y. Zeng, S. J. Jiang, X. Y. Gong and J. L. You, *Inorg. Chem.*, 2019, **58**, 5025–5030.

15 X. S. Lv, Y. L. Sun, X. L. Tang, S. M. Wan, Q. L. Zhang, J. L. You and S. T. Yin, *J. Cryst. Growth*, 2013, **371**, 107–111.

16 D. Elwell and H. J. Scheel, *Crystal Growth from High-Temperature Solutions*, Academic Press, London, UK, 1975.

17 C. T. Sun and D. F. Xue, *CrystEngComm*, 2016, **18**, 1262–1272.

18 F. Nishi, *Acta Crystallogr., Sect. C: Cryst. Struct. Commun.*, 1997, **53**, 399–401.

19 J. P. Guha, D. Kolar and A. Porenta, *J. Thermal Anal.*, 1976, **9**, 37–41.

20 O. Yamaguchi, H. Sasaki, K. Sugiura and K. Shimizu, *Ceram. Int.*, 1983, **9**, 75–79.

21 K. Refson, P. R. Tulip and S. J. Clark, *Phys. Rev. B: Condens. Matter Mater. Phys.*, 2006, **73**, 155114.

22 V. Milman, K. Refson, S. J. Clark, C. J. Pickard, J. R. Yates, S. P. Gao, P. J. Hasnip, M. I. J. Probert, A. Perlov and M. D. Segall, *J. Mol. Struct.: THEOCHEM*, 2010, **954**, 22–35.

23 J. P. Perdew and A. Zunger, *Phys. Rev. B: Condens. Matter Mater. Phys.*, 1981, **23**, 5048–5079.

24 D. R. Hamann, M. Schlüter and C. Chiang, *Phys. Rev. Lett.*, 1979, **43**, 1494–1497.

25 D. Porezag and M. R. Pederson, *Phys. Rev. B: Condens. Matter Mater. Phys.*, 1996, **54**, 7830–7836.

26 C. M. Foster, M. Grimsditch, Z. Li and V. G. Karpov, *Phys. Rev. Lett.*, 1993, **71**, 1258–1260.

27 A. V. Krukau, O. A. Vydrov, A. F. Izmaylov and G. E. Scuseria, *J. Chem. Phys.*, 2006, **125**, 224106.

28 T. M. Henderson, J. Paier and G. E. Scuseria, *Phys. Status Solidi B*, 2011, **248**, 767–774.

29 J. Tauc, R. Grigorovici and A. Vancu, *Phys. Status Solidi B*, 1966, **15**, 627–637.

30 P. Makuła, M. Pacia and W. Macyk, *J. Phys. Chem. Lett.*, 2018, **9**, 6814–6817.

31 C. Kittel, *Introduction to Solid State Physics*, John Wiley & Sons, New Jersey, USA, 2005.

32 H. N. Li, T. Baikie, S. S. Pramana, J. Felix Shin, P. J. Keenan, P. R. Slater, F. Brink, J. Hester, T. An and T. J. White, *Inorg. Chem.*, 2014, **53**, 4803–4812.

33 S. J. Jiang, S. M. Wan, W. Luo, B. Li and J. Y. Yao, *J. Mater. Chem. C*, 2022, **10**, 649–654.

34 E. Kroumova, M. I. Aroyo, J. M. Perez-Mato, A. Kirov, C. Capillas, S. Ivantchev and H. Wondratschek, *Phase Transitions*, 2003, **76**, 155–170.

This journal is © The Royal Society of Chemistry 2024

J. Mater. Chem. C, 2024, **12**, 17122–17127 | **17127**